MÁSTER EN ASTROFÍSICA

TRABAJO DE FIN DE MÁSTER

KINEMATICS OF VIRTUAL GALAXIES FROM THE EAGLE SIMULATION

Author: Daniel Walo Martin

Director: Jesús Falcón Barroso

Codirector: Claudio Dalla Vecchia

Index

1. Resumen

Los avances realizados en el desarrollo de espectrógrafos de campo integral han permitido no sólo obtener medidas de alta resolución en 2D de la cinemática estelar de galaxias sino estudiar cómo se ve afectada por factores como la masa estelar, color y el ritmo de formación estelar entre otros. La realización de *surveys* como SAURON, ATLAS^{3D}, ManGA y CALIFA ha permitido analizar un gran número de galaxias (de tipo temprano en su mayoría) y clasificarlas en *slow* y *fast rotators* en función de su momento angular y elipticidad aparentes. Estas técnicas están limitadas a estudiar galaxias en el universo cercano ya que es muy difícil medir la señal de las estrellas de galaxias a alto corrimiento al rojo. Por lo tanto, el análisis de la cinemática estelar de galaxias en distintas épocas del universo sólo se puede llevar a cabo a partir simulaciones

En este trabajo se analiza la cinemática de galaxias de EAGLE cuyos resultados han sido liberados al público general hace un año. EAGLE es un conjunto de simulaciones a escala cosmológica que analiza la evolución e interacción de un número estadísticamente significativo de galaxias. Para ello se ha desarrollado un conjunto de scripts que permiten analizar los datos de EAGLE de manera sencilla al que hemos llamado *EKA* (EAGLE Kinematic Analysis). Se han obtenido los mapas de velocidad y dispersión de velocidades y se ha analizado la relación entre el momento angular y elipticidad aparentes para distintos instantes de tiempo. Los resultados obtenidos muestran un buen acuerdo con otros trabajos similares en la literatura y con las observaciones. Además, se ha comprobado la evolución con el tiempo del momento angular aparente y la fracción de energía cinética en contrarotación analizando los resultados de EAGLE para distintos corrimientos al rojo.

2. Introduction

Galaxies are commonly classified into fast and slow rotators according to their kinematic properties. These terms were coined by Emsellem et al. (2007), after observing that the stellar kinematic is not strongly correlated with the distribution of stars in early type galaxies using integral field spectroscopy (IFS) results from SAURON (Bacon et al. 2001). In this work, the authors showed that morphology is not necessarily a good indicator of the dynamics of galaxies and proposed the apparent angular momentum λ_R as a new scheme to classify galaxies. This parameter measures how rotationally or dispersion-dominated a galaxy is. The first criteria to classify galaxies as fast or slow rotators was a threshold value of $\lambda_R = 0.2$ in Emsellem et al. (2007). Recent works have proposed more sophisticated criteria were the apparent ellipticity of the galaxy also plays a role (e.g. Emsellem et al. 2007 and Cappellari et al. 20011).

The angular momentum is a key parameter to understand not only kinematic properties of galaxies but also their evolutionary path. This parameter is set in the early life stages of galaxies, providing an important tool to distinguish between different scenarios of galaxy evolution. For example, is believed that the amount of angular momentum transferred from halo to disk provides constraints to the size of the galactic disk (Mo et al. 1998) and to set the basis for the mass-size relation of galaxies (Shen et al. 2003). Moreover, the angular momentum provides a possible explanation of the observed morphology-density relation, by means of spiral galaxies transformation into fast rotating lenticular galaxies through fading of the stellar population (e.g. Capellari et al. 2011).

Recent IFS surveys such as ATLAS^{3D} (Cappellari et al. 2011), SAMI (Croom et al. 2012; Bryant et al. 2015), ManGA (Mo et al. 1998) and CALIFA (Sánchez et al. 2012) have explored how the resolved kinematics of the stars and ionised gas relate to global galaxy properties, such as stellar mass, colour, star formation rate (SFR) and environment, among others. The most important aspect is that they observe the order of hundreds to thousands galaxies enabling the galaxy population to be dissected into many properties. However, most of them are focused in the study of early type galaxies being CALIFA the only survey that observes galaxies across the Hubble sequence.

Additionally, the surveys above only observe galaxies in the nearby universe (e.g. the maximum redshift is $z{\sim}0.03$ for the ManGA survey) due to the great difficulties of detecting the spectra of distant galaxies. There are higher-z surveys ($z{\sim}1-3$) such as KMOS (Sharples e al. 2006) and SINS (Förster-Schreiber et al. 2009) but are based on the detection of emission lines from gas. The latter technique do not provide information about the real stellar kinematic of the galaxies since gas is affected by different mechanism with time scale are much shorter. Therefore, the only way to study the stellar kinematic properties of galaxies is through simulations.

After SAURON and ATLAS^{3D} results a great number of simulations and theoretical work was developed to understand the evolutionary path of slow and fast rotators (e.g. Jesseit et al. 2009, Bois et al. 2011 and Naab et al. 2014). These studies found important results about the influence of galaxy mergers in the formation of slow and fast rotators but the small volume of the simulations struggled in analysing the effect of environment and in having a statistically unbiased representation of different formation pathways.

Recently, new cosmological simulations volumes have been able to produce realistic galaxy populations thanks to improved subgrid models for unresolved feedback processes and the ability to run large cosmological volumes with sub-kiloparsec resolution. Examples of these simulations include EAGLE (Schaye et al. 2015), Ilustris-TNG (Pillepich et al. 2017) and Horizon-AGN (Dubois et al. 2014). These simulations reproduce the morphological diversity of galaxies, the galaxy colour bimodality and the stellar and the stellar mass function among other features

observed in the local Universe (e. g. Furlong et al. 2015; Genel et al. 2014; Snyder et al. 2015; Dubois et al. 2016)

In this work, we will analyse the results from EAGLE simulation which have been publicly released last year. It has been shown that EAGLE is able to reproduce observational results such as the size-stellar mass relation (Furlong et al. 2016; Katsianis et al. 2017) and the specific angular momentum-stellar mass relation (Lagos et al. 2017; Swinbank et al. 2017) through time which demonstrates the ability of the simulation to reproduce structural and dynamical properties of galaxies. In addition ,EAGLE also reproduces the evolution of SFR properties of galaxies (Furlong et al. 2015), colours (Trayford et al. 2015), and produces both a blue cloud of predominantly disky galaxies and a red sequence of mostly elliptical galaxies (Correa et al. 2017). On the contrary, there are some discrepancies between the simulation results and observational data. In particular, it has been found that the stellar mass density is approximately 20% lower than inferred from observations (Schaye et al. 2015, Furlong et al. 2016), present day stellar mass-metallicity relation in some models is flatter than the one inferred from observational data (Schaye et al. 2015) and the transition from active to passive galaxies occurs at too high stellar mass at z=0 (Schaye et al. 2015, Trayford et al. 2015).

The kinematical properties of EAGLE has not yet been fully analysed and only few studies on this topic can be found in the literature. EAGLE offers the possibility of analysing the evolution of stellar kinematics of a statistically significant set of galaxies in cosmological volumes as it has never been done before. In addition, the results of this work could bring a new light into understanding the origin of different kinematics features observed in our universe.

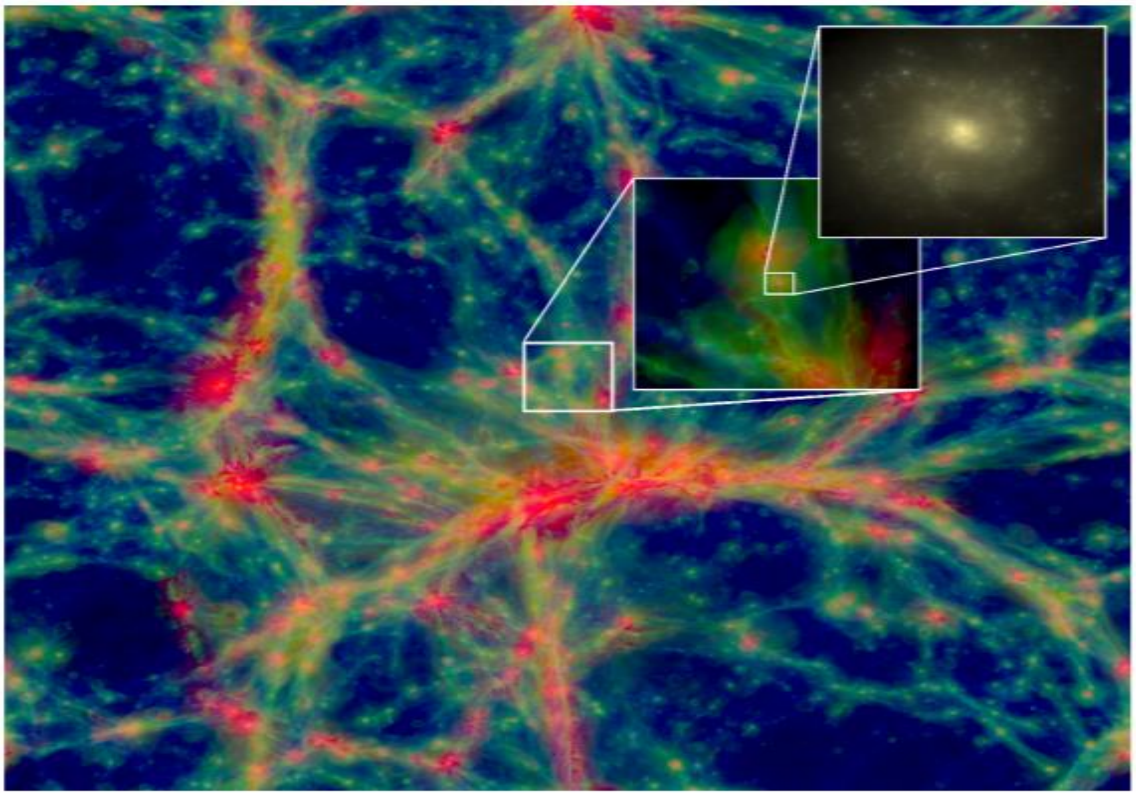

Figure 0. A 100×100× 20 slice of the RefL0100N1504 simulation at z=0. The inset shows regions of 10 cMpc and 60cMpc on a side and zoom into an individual galaxy. Taken from (Schaye et al. 2015)

3. Objectives

The main objective of this work is to develop computational tool to measure and analyse the kinematic properties of galaxies from EAGLE simulations. The specific aims of this work are:

- To develop scripts to analyse the kinematical properties of EAGLE simulations.
- To obtain kinematic maps of EAGLE galaxies.
- To measure the apparent angular momentum, λ_R.
- To compare EAGLE λ_R diagrams with results from surveys.
- To analyse the correlations of λ_R with different parameters.
- To analyse the evolution of λ_R through time.

4. Methodology

This section is divided in three different parts. We first present EAGLE key aspects and how the database and particle data are structured. Then, we describe how the projected images and kinematic maps are obtained. Finally, we explain the structure of our scripts.

4.1. The EAGLE simulation

EAGLE (Evolution and Assembly of Galaxies and their Environments) is a project from the Virgo Consortium that consists of a suite of cosmological hydrodynamical simulations aimed at understanding how galaxies form and evolve. These simulations assume a Λ Cold Dark Matter (ΛCDM) universe, adopting the cosmological parameters derived from Planck mission (Planck Collaboration et al. 2014). These parameters are shown in Table 1. An important aspect of EAGLE is the use of state-of-the-art sub-grid modules that account for physical processes below the resolution scale of the simulation such as radiative cooling and photoheating (Wiersma et al. 2009a), star formation (Schaye & Dalla Vecchia 2008), stellar evolution (Wiersma et al. 2009b), chemical enrichment (Dalla Vecchia & Schaye 2008) and black hole growth and active galactic nucleus (AGN) feedback (Rosas-Guevara et al. 2015).

Ω_m	Ω_Λ	Ω_b	h	σ_8	n_s	Y
0.307	0.693	0.04825	0.6777	0.8288	0.9611	0.248

Table 1. Parameters of a ΛCDM universe derived from the Planck mission. From left to right: cold dark matter density, dark energy density, baryon density, dimensionless Hubble parameter, density fluctuations, scalar spectral index and primordial helium abundance.

Simulations were performed in cubic volumes with lengths of L= 12, 25, 50 and 100 co-moving mega-parsec (cMpc hereafter). Simulations are referred to as 'high resolution' or 'intermediate resolution' according to their initial baryonic particle mass, $m_g = 2.26 \cdot 10^5 M_\odot$ and $m_g = 1.81 \cdot 10^5 M_\odot$ respectively. The maximum gravitational softening lengths are $\epsilon_{prop} = 0.35$ proper kilo-parsec (pkpc hereafter) for the high resolution simulation and 0.7 pkpc for the intermediate resolution simulation. The code switches to a softening length that is constant, ϵ_{com}, in co-moving coordinates at $z \geq 2.8$.

The EAGLE suite comprises runs where some of the subgrid modules, or parameters of these modules, were changed for the same volumes and resolutions. For example, in the REFERENCE simulation the numerical parameters of the subgrid modules were calibrated to a limited subset of z=0 observations of galaxies: galaxy stellar mass function, galaxy sizes and black hole mass – stellar mass relation. Other models are not recalibrated, e.g. WEAK and STRONG models, or use slightly different subgrid parameters for high resolution simulations as RECAL.

The naming convention adopted for the EAGLE simulations uses the model of the subgrid modules, the volume of the simulation and the number of initial dark matter and gas particles. For example the REFL0025N0376 refers to a simulation with REFERENCE subgrid modules, L = 25cMpc that starts with $2x376^3$ particles of dark matter and gas. Particle data are output in snapshots,-the state of the system at a given redshift-, at different redshifts. There are 29 snapshot for each simulation ranging from z=20 to z=0. Each snapshot is distributed over several files, and to extract all particles from a given snapshots we must read all files. Snapshots can be downloaded at http://icc.dur.ac.uk/Eagle/database.php after registration. Haloes are identified in the simulation using the Friends-of-Friends (FoF hereafter) and spherical algorithms while galaxies are identified as self-bound structures using the SUBFIND algorithm (Dolag et al. 2009). Particles in a FoF halo are tagged with a *GroupNumber* that runs from 1 to N (total number of groups). Particles within a halo in a self-bound substructure are tagged with a *SubGroupNumber*, which

ranges from 0 (the main galaxy in this FoF group) to N-1 (where N is the number of subgroups). Particles with *GroupNumber* or *SubGroupNumber* equal to 2^{30} do not belong to any group or subgroup. It must be taken into account that *GroupNumber* and *SubGroupNumber* refer to a given snapshot and generally will not refer to the same physical structures in different snapshots.

Individual snapshot files are written in the binary HDF5 format and each file contains a set of groups with information about the simulation and the particle data. Particle properties are written in groups PartType0 to PartType5. In Eagle type 0 are gas particle, type 1 are dark matter particles, type 4 are stellar particles and type 5 are supermassive black holes. Types 2 and 3 are not used. The hdf5 groups used in this project are the *Header*, *Parameters* and *PartType4*. The *Header* group contains the standard simulation parameters: *boxsize* (length of the cubic volume of the simulation), *Omega0* (Ω_0, the total matter density in units of the critical density), *OmegaLambda* (Ω_Λ, density parameter corresponding to the cosmological constant), *OmegaBaryon* (Ω_b, mean baryon density in units of the critical density) the HubbleParam and the *ExpansionFactor* the current value of the expansion factor, $a = 1/(1+z)$, at the redshift of the snapshot. The *Parameters* group have a list with the primordial and solar abundances of 9 chemical elements (H,He,C,Ni,0,Ne,Mg,Si,Fe) and the assumed metallicity of the Sun, $Z_\odot$.The *PartType0-5* groups have different number of variables but they all have in common the mass, position, velocity and unique particle identifier attributes (snapshot ParType0-5 group variables *Mass*, *Coordinates*, *Velocity* and *ParticleIDs*) regardless of particle type. Star attributes used in this study will be discussed in the next section. For further information of variables in the PartType groups see Tables 4-7 of EAGLE team (2017).

The Virgo Consortium has also publicly released a catalogue of galaxies and haloes main properties in the form of an SQL database (McAlpine et al. 2016). The database can be accessed from the same web where the simulation snapshots are downloaded. At each redshift the galaxies are processed one by one to obtain the quantities stored in the database. Some quantities require a simple summation over the particles e.g. mass and metallicity but other quantities such as luminosities in various filters require more complex calculations that cannot be directly calculated from the snapshots. For each simulation the EAGLE database has information distributed across five SQL tables except the Ref simulations which has six tables. The name and description of the tables in the database are shown in Table 2.

SQL Table name	Contents
Subhalo	Main galaxy properties
FOF	Halo properties
Sizes	Galaxy sizes
Apertures	Galaxy properties in 3D apertures
Magnitudes	Galaxy photometry in GAMA bands
Stars (only available for Ref simulations)	Masses, ages, metallicities and magnitudes of star particles in a snapshot

Table 2. SQL tables for each simulation

Galaxies are identified in the database with the variable *GalaxyID* along with the *GroupNumber* and *SubGroupNumber*. This value is unique but is linked to a snapshot and thus it cannot be used to study the same galaxy in different snapshots.

Cosmological simulations like EAGLE enable to study the evolution of physical magnitudes of galaxies through time. To do so, we must construct the merger tree of a galaxy and study the properties of its progenitors and descendant galaxies. In EAGLE, the main branch of a merger tree is defined as the lineage with the highest cumulative mass. These trees can be really complex since galaxies may experience a great number of mergers but they can be easily travelled through the database using three more identifiers: *TopLeafID* (*GalaxyID* of the highest-redshift main

branch progenitor), *LastProgID* (maximum *GalaxyID* of all progenitors irrespective of their branch) and *DescendantID* (*GalaxyID* of the unique descendant galaxy of the actually chosen galaxy. All the galaxies in the main progenitor branch of a galaxy with *GalaxyID* i and *TopLeafID* j have a *GalaxyID* in the range [i,j] in ascending redshift order.

4.2. Kinematic measurements

Kinematic properties are obtained from projected images of the galaxies. These images are calculated by projecting the stellar particle position onto a 2-D plane. This process requires handling both the snapshot files and the database.

To construct the maps, we first set the centre of potential of the galaxy as the rest frame of the snapshot. The centre of potential is available in the database (*CentreofPotential_x/_y/_z* variables) and it represents the position of the most bound particle and it is always at the centre of the galaxy. The centre of mass is also a database variable and usually it's almost equal to the centre of potential but it can lead to Field-of-View (FoV hereafter) misalignment because it's a parameter more sensitive to merger interaction and tidal forces.

The next step is to define the size of the projected 2-D image by selecting the number of pixels and their size. We choose an equal number of square pixels, N_{pixels}, of length l pkpc in both directions leading to a square FoV of size 2Lx2L pkpc, where 2L is the length of the FoV. The center of the FoV is aligned with the rest frame and thus all the particles between [-L, L] in both directions will appear in the final image. Each particle in the 2D-image is tagged with the row and column numbers of the pixel that they belong to. The line-of-sight is along the x-axis and we use two orientations to obtain the maps: a random view and an edge-on view, in which the stellar spin is oriented along the z-axis. To obtain the edge-on view we use the spin vector of the stars, $\vec{S}$, and rotate the galaxy to orient it along the z axis. We calculated this parameter similar to the database, using expression (1), including only those particle within a 15 pkpc radius spherical aperture centred at the centre of potential to reduce the effect of high velocity particles from mergers.

$$\vec{S} = \frac{\sum_i m_i (r_i - r_{CP}) \times (v_i - v_{CP})}{\sum_i m_i} \quad (1)$$

where m_i, r_i and v_i are the mass, position and velocity of the particle and r_{CP} and v_{CP} are the position and velocity of the centre of potential. The velocity of the centre of potential is not provided in the database so we assume that it's equal to the velocity of the centre of mass

Kinematic information is recovered from the distribution of velocities of stellar particles along the line of sight, the Line of Sigh Velocity Distribution (LOSVD hereafter). In EAGLE we have direct access to the velocity of each individual stellar particle and we can easily construct a LOSVD with the particles in each pixel. However, we need to do some additional steps to compare our results with observational data.

First, we filter the projected image and keep those pixels with number of particles greater than a fixed threshold, Nmin, and perform a Voronoi binning (Cappellari & Copin 2003) to reach a minimum target signal to noise, S/N. We take the number of particles per pixel as the signal and assume that their distribution follows a Poisson distribution. Therefore, the S/N in each pixel is equal to the square root of particles in it. Voronoi binning is a tool frequently used in IFS to obtain the LOSVD from galaxy spectra using spectral libraries like MILES (Vazdekis et al. 2010) and deconvolution techniques such as Penalized Pixel-Fitting (pPXF) (Cappellari & Emsellem 2004). The initial filter is applied to avoid non connected regions in the image.

In observations the LOSVD is a luminosity-weighted distribution since we get more information from the brightest stars. Therefore, we weigh the contribution of each stellar particle according to its luminosity. EAGLE snapshots do not provide the luminosity of the stellar particles, but we can get it through different methods. The REFERENCE models have an extra table in the database, *Stars*, with the magnitude in different filters of all the stellar particles. However, this option was discarded since it limits the use of our scripts to the REFERENCE model and because it would require managing another set of files that would slow down the performance of our codes. We decided to use EMILES stellar population synthesis models to obtain luminosities in the g band from the metallicity and age of the stellar populations.

Metallicities are available in the snapshot *ParType4* group and are given as mass fractions while EMILES models define metallicity as the ratio of metal mass over hydrogen mass relative to the sun. Therefore, we transform EMILES metallicities into mass fractions before interpolating.

On the other hand, stellar age is not a snapshot variable but it can be calculated from the age of the universe at the redshift when the particle was created minus the age of the universe at the redshift we are considering. In a ΛCDM universe the age of the universe as a function of the expansion factor can be calculated using equation (2)

$$Time(a) = \frac{2t_h}{3\sqrt{\Omega_\Lambda}} \log\left(\sqrt{\frac{\Omega_\Lambda}{\Omega_0}} a^{3/2} + \sqrt{\left(1 + \frac{\Omega_\Lambda}{\Omega_0}\right) a^3} \right) (Gyr) \tag{2}$$

where t_h is the Hubble time in Gyr. Thus, using the ParType4 group variable *StellarFormationTime* (the value of the expansion factor at the time the particle was created) and the expansion factor of the universe from the *Header* group we can obtain the age of the stars.

To calculate the mean velocity, V, and velocity dispersion, σ, in each Voronoi bin we calculate the luminosity-weighted mean value and standard deviation of stars velocities. We also fit the LOSVD to a Gauss-Hermite distribution (3). This analysis was first introduced by (van der Marel & Franx 1993) to analyse the LOSVD from early type galaxies. This models introduces the h_3 and h_4 coefficients that account of distribution deviations from a Gaussian, skewness and kurtosis respectively. Additionally, disc galaxies can be easily identified using this method through the $V - h_3$ negative correlation.

$$F(w) = \frac{1}{3\sqrt{2\pi\sigma^2}} \exp\left(-\frac{1}{2w^2}\right)\left(1 + \frac{h_3}{\sqrt{3}}(2w^3 - 3w) + \frac{h_4}{\sqrt{24}}(4w^4 + 3w^2 - 12)\right) \tag{3}$$

$$w = \frac{v - V}{\sigma}$$

where V is the mean velocity, σ is the velocity dispersion and h_3 and h_4 are the Gauss-Hermite coefficients that describe the level of skewness and kurtosis.

Both approaches provide a velocity that includes the systemic velocity of the galaxy. To eliminate this contribution we subtract the mean velocity inside a box of 4x4 spatial bins at the centre of the velocity map.To classify galaxies into fast and slow rotators we calculate the apparent angular momentum, λ_R, and ellipticity, ϵ, to construct the $\lambda_R - \epsilon$ diagrams.

To measure the ellipticity we diagonalize the inertia tensor of the galaxy's luminosity. We obtain the ellipticity as:

$$\epsilon = 1 - \sqrt{\frac{a}{b}} \tag{4}$$

where

$$a = \frac{\bar{x}^2 + \bar{y}^2}{2} + \sqrt{\left(\frac{\bar{x}^2 - \bar{y}^2}{2}\right)^2 + \overline{xy}^2} \tag{5}$$

$$b = \frac{\bar{x}^2 + \bar{y}^2}{2} - \sqrt{\left(\frac{\bar{x}^2 - \bar{y}^2}{2}\right)^2 + \overline{xy}^2} \tag{6}$$

and

$$\bar{x}^2 = \frac{\sum_i L_i x_i^2}{\sum_i L_i}, \qquad \bar{y}^2 = \frac{\sum_i L_i y_i^2}{\sum_i L_i}, \qquad \overline{xy} = \frac{\sum_i L_i x_i y_i}{\sum_i L_i} \tag{7}$$

Here, a and b are the eigen values of the inertia tensor which are proportional to the square values of the semiaxes. The index i corresponds to the stellar particles inside the aperture in which we wish to measure the ellipticity. We also calculate the position angle of the major axis of the galaxy (measured counter clockwise from y=0) as:

$$\theta_{PA} = \frac{1}{2}\text{atan}\left(\frac{2\overline{xy}}{\bar{x}^2 - \bar{y}^2}\right) \tag{8}$$

We calculate the ellipticity within a circular aperture of radius R_{50}, the radius of the circular aperture that includes half the luminosity within it, as in previous studies (e.g. Emsellem et al. 2007). However, these measurements are strongly affected by non-axisymmetric distortions caused by structures such as bars or spiral arms and the value obtained may not account for the real shape of the projected galaxy. To minimize these effects we also calculate the ellipticity inside an annular mask of a few pkpc around R_{90}, the radius that contains 90% of the luminosity.

We calculate the apparent angular momentum following Emsellem et al. (2007) as:

$$\lambda_R = \frac{\sum_j^N L_j R_j |V_j|}{\sum_j^N L_j R_j \sqrt{V_j^2 + \sigma_j^2}} \tag{9}$$

where L_j, R_j, V_j and σ_j are the luminosity, circular radius, mean velocity and velocity dispersion per spatial bin in the projected maps. The summation over the j index includes the Voronoi bins within an elliptical aperture of major semi-axis R, ellipticity, ϵ, and position angle θ_{PA}. We calculate λ_R for elliptical apertures of major semi-axis R_{50} and R_{90}.

The apparent angular momentum is the only parameter that we calculate from the maps while the rest of them are calculated directly from the particle data. In this way we obtain measurements independent of the FoV spatial resolution. To analyse the properties of λ_R and how it correlates with other properties we also calculate the age, metallicity, Z, and magnesium over iron, [Mg/Fe], luminosity weighted average values within the same elliptical apertures.

Another important analysis is the relation between the Hubble type of the galaxies and their apparent angular momentum. Using EAGLE simulations we could understand how different kinematic properties evolve through time and what is the role of λ_R in the formation of each different type. Morphology classification is typically carried out either by an extensive visual inspection (e.g. Galaxy Zoo project, Lintott et al. 2011) or through the stellar kinematics (Emsellem et al. 2007) but both methods cannot be implemented in our analysis because the number of galaxies is too high to visually inspect all the maps. However, there is another method

that can be used to determine whether a galaxy is bulge or disc dominated using the fraction of kinetic energy invested in ordered corotation (Correa et al. 2017),

$$\kappa_{corot} = \frac{K_{corot}}{K} = \frac{1}{K}\sum_{i}^{r<R}\frac{1}{2}m_i\left[\left(\frac{L_{z,i}}{m}_i R_i\right)\right]^2 \quad (10)$$

where the sum is over all stellar particles within a spherical radius R centred at the centre of potential that follow the direction of rotation, m_i is the mass of each stellar particle, $K\left(=\sum_i^{r<R}\frac{1}{2}m_i v_i^2\right)$ the total kinetic energy, $L_{z,i}$ the particle angular momentum along the direction of the total angular momentum of the stellar component of the galaxy $\vec{L}$ and R_i is the projected distance to the axis of rotation. Based on visual inspection of a larger number of galaxies κ_{corot}=0.4 was picked to separate galaxies that look disky (κ_{corot}<0.4) from those that look elliptical (κ_{corot}>0.4).

Different from the literature, we reduced the radius of the spherical volume where we measure κ_{corot} from 30 to 15 pckp since it's the same volume that we used to compute the stellar spin for the edge-on view.

Additionally, we also calculate the fraction of kinetic energy invested in counter-rotation, $\kappa_{counter}$, in a similar way to κ_{corot} but considering the stellar particles that go in opposite direction to the direction of rotation. This parameter is quite interesting because the level of counter rotation in a galaxy is linked with the number of merger interactions that galaxies have undergone. In observations, mergers are very difficult to measure using photometry unless the interaction has recently occur and in the kinematic maps there's usually a dominant component that makes it impossible to measure the counter rotating velocities.

4.3. EAGLE Kinematic Analysis (EKA)

4.3.1 General aspects

To analyse EAGLE snapshots we have developed *EAGLE Kinematic Analysis* (*EKA* hereafter), a series of scripts written in Python 3.6.5. *EKA* consists of two scripts: *EKA_main* where all the calculations are performed and *EKA_utils* where the auxiliary functions used by *EKA_main* are collected. *EKA_main* is programmed using object oriented programming to facilitate the analysis of different EAGLE simulations. To program these scripts we have used the libraries Numpy, Scipy, glob, h5py, astropy and statsmodels. We have implemented all the functions gathered in *EKA_utils* except the functions to read the snapshot files taken from EAGLE team (2017), and the Voronoi binning algorithm, downloaded from http://www-astro.physics.ox.ac.uk/~ mxc/software/.

EKA scripts require one extra file that includes parameters from the database. Some of these parameters are used along the script to select the stellar particles and generate the maps, e.g. *GroupNumber* and *SubGroupNumber* but most of them are global properties of the galaxies not involved in the calculations. The latter are directly saved into the output file to facilitate the analysis of the results. This file determines the number of galaxies analysed in the *EKA_main* script. The parameters in this file are shown in Table 3.

The *EKA_main* script accesses to the *Header*, *Parameters* and *Partype4* groups to perform the analysis. From the *Header* group we get *Omega0*, *OmegaLambda* and *ExpansionFactor* variables to calculate the age of the stellar particles using (2). To calculate the mean values of metallicity and [Mg/Fe] relative to solar values we use the *Parameter* group and get the estimated solar abundances and metallicity. Stellar particle information is acquired from the *PartType4* group. A complete list with the *PartType4* variables used in the analysis is shown in Table 4.

Parameter name	Units	Brief Description
GroupNumber *SubGroupNumber*	-	Unique identifiers of a galaxy that enables the connection between the database and the snapshots
GalaxyID *LastProgID* *TopLeafID* *DescendantID*	-	Unique identifiers of galaxies used to travel the merger tree.
CentreofPotential_x *CentreofPotential_y* *CentreofPotential_z*	$cMpc$	Co-moving position of the centre of potential
Velocity_x *Velocity_y* *Velocity_z*	Km/s	Peculiar velocity
MassType_Star *MassType_DM* *MassType_Gas* *MassType_BH*	$M_{\odot}$	Total stellar mass Total dark matter mass Total gas mass Total black hole mass
StarFormationRate	$M_{\odot}/year$	Total star formation rate

Table 3. Database parameters used in the *EKA* scripts. All the parameters are in the *Subhalo* table.

Each analysis is characterised by the six input parameters of the *EKA_main* class. These parameters are:

-*snappath*: path to the snapshot files.

-*EdgeOnview:* boolean type variable. The galaxy is studied in edge-on view if *True* and in random view is *False*.

-*Npixels*: Number of spatial bins in the 2D images.

-*Lpixel*: Size of spatial bins in the 2D images.

-*Nmin:* Minimum number of stars per pixel required to analyse the pixel

-*SNtarget*: Value of the signal to noise in the Voronoi binning.

EKA provides a set of maps and global parameters for each galaxy that are saved into a single hdf5 file. This file contains three groups described below.

-Header group

Includes the input parameters of the *EKA_main* class that characterize how the analysis was carried out.

-General_Output group

Contains the global parameters of the galaxies either provided by the input database file or calculated from the particle data. Most of these parameters have been measured within elliptical apertures of major semiaxis R_{50} and R_{90} weighted by the mass and luminosity of the stars. The complete list and description of the parameters in this group is shown in Table A1.

-Maps group

This group has the information of the maps obtained in the *EKA_main* calculation process. There is a total of N subgroups, being N the number of galaxies analysed. The name of each subgroup is the GalaxyID of the galaxy. The complete list of maps for each galaxy is shown in Table A2.

Variable name	Description
GroupNumber	Group number of the galaxy this particle belongs to
SubGroupNumber	Subgroup number of the galaxy this particle belongs to
Coordinates	Co-moving coordinates
Velocity	Peculiar velocity
Mass	Particle mass
Metallicity	Mass of elements heavier than Helium, divided by particle mass
ElementAbundance/Magnesium	Mass of Magnesium divided by particle mass
ElementAbundance/Iron	Mass of Iron divided by particle mass
StellarFormationTime	Expansion Factor when this star was born

Table 4. Variables from the *PartType4* group used in the *EKA_main* script.

4.3.2. Script performance

To analyse a galaxy we first have to identify which stellar particles belong to it. Each time we get a parameter from the *PartType4* group we load the information of all the stellar particles in the simulation. First, we load the *GroupNumber* and *SubGroupNumber* of all the stellar particles in the snapshot. Then, we construct a mask to select those particles with same *GroupNumber* and *SubGroupNumber* as the galaxy we want to analyse and use it to select the target particles each time we load another parameter. Reading the snapshot files is a time consuming action and this is not a viable approach when we want to analyse a large set of galaxies.

To study big sets of galaxies we load the *GroupNumber* and *SubGroupNumber* of all the stellar particles and create a mask that includes the particles of all the galaxies that are going to be analysed. Next, we load all the parameters listed in Table 4 and filter them using this mask, including the *GroupNumber* and *SubGroupNumber* parameters. Then, for each galaxy we create a secondary mask from the filtered *GroupNumber* and *SubGroupNumber* and we apply it to the rest of the filtered quantities. This procedure requires more memory but improves the performance of the script. For example, it takes 2 hours to analyse 360 galaxies accessing the snapshot files for each galaxy and only 15 minutes if all the information is loaded at the beginning.

Once the stellar particles have been selected we follow the next steps:

1º) Set the centre of potential of the galaxy as the rest frame. Transform coordinates and velocities of the stellar particles.

2º) Calculate the stellar spin of the galaxy and rotate the galaxy to edge on configuration if applicable.

3º) Project the stars into a 2D image.

4º) Select pixels with signal above the minimum number of particles threshold.

5º) Apply the Voronoi binning routine.

6º) Calculate the following parameters for each Voronoi Bin:

- Number of stars

- Stellar Mass

- Luminosity

- Mass and luminosity weighted mean velocity

- Mass and luminosity weighted mean velocity dispersion

- Gauss-Hermite coefficients from mass and luminosity weighted LOSVD

- Mass and luminosity weighted mean stellar age

- Mass and luminosity weighted mean metallicity

- Mass and luminosity weighted mean magnesium over iron

7º) Calculate R_{50} and R_{90}.

8º) Calculate ellipticity and position angle within R_{50} and around $R_{90}$from luminosity and mass maps.

9º) Calculate λ_R in elliptical apertures within $R_{50}$and $R_{90}$from luminosity and mass derived velocity and velocity dispersion maps.

10º) Calculate the rest of the parameters from Table 5.

11º) Create a subgroup in the *Maps* group and save the maps

Steps 4º and 5º may give rise to errors in the script and stop the analysis. We have taken measures to prevent three different situations:

- There are no pixels with signal above the fixed N_{min} threshold. The galaxy is not analysed. This situation arises with galaxies with few stars or when the threshold value is too big.

- Image data is too noisy. The Voronoi binning algorithm is unable to process it. The galaxy is not analysed.

-The minimum S/N in the image is greater than the target S/N of the Voronoi binning. The algorithm returns and error since it's not necessary to apply it. We set the target S/N of the Voronoi binning to the minimum S/N plus one.

To construct the LOSVD in step 6º we set the number of bins equal to the square root of the number of particles in the Voronoi bin. The LOSVD is normalized to avoid including an extra normalization parameter to eq. (3) in the fitting process.

In steps 6º and 7º we calculate metallicity and magnesium over iron mean values. These quantities are typically given relative to solar values in logarithmical scale. There are some particles with magnesium and iron abundances equal to cero. These particles also have cero metallicity values and represent the oldest star populations that haven't undergo Type Ia and Type IIa supernovas. We set their Mg/Fe to zero to avoid numerical problems. There are also some stars with small magnesium abundance and really small iron abundance (twenty five orders of magnitude smaller than magnesium abundance on average). The number of these stars is really

small but their value is so high that the rest of the particles have almost no impact in the mean value. The origin of this values is not yet well understood, it could either be an error in the subgrid modules or a physical process that we have not yet understood. Therefore, the mean Mg/Fe is calculated as the mean value of the logarithm of Mg/Iron ratio of each particle to reduce the contribution of these odd particles.

In Figure 1 we show a flow diagram that summarises *EKA* analysis process.

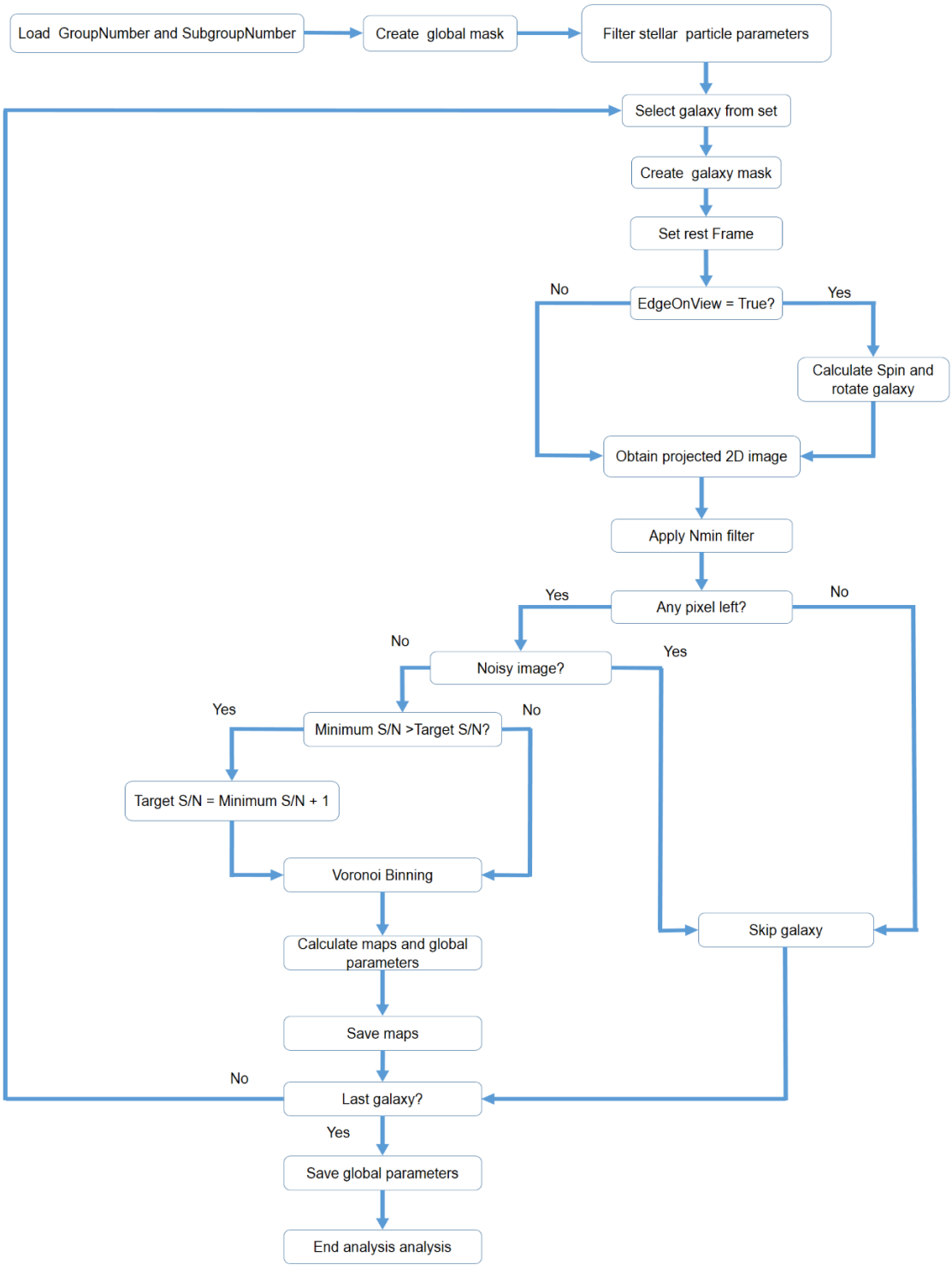

Figure 1. Flow chart of the *EKA* analysis process.

5. Results

In this section we show the results of applying *EKA* scripts to analyse EAGLE simulations. First, we explain which simulations have been studied and how they were analysed. Next, we show which kinematic measurement method has been selected. Then, we show how our results agree with other works in the literature. Next, we show different types of galaxies according to their kinematic maps. After that we present the $\lambda_R - \epsilon$ diagrams and compare it with other diagrams from IFS surveys. Finally, we present the evolution of lambda R through time.

5.1. Analysis

We have used EKA scripts to analyse RefL0100N1504 simulation at different redshift. We have included in the analysis galaxies with stellar mass greater than $10^{10} M_{\odot}$. Additionally we have studied RefL0050N0752 at redshift 0 to compare our kinematic maps with those found in Lagos et al. (2018). We chose Ref simulations because their subgrid modules have been calibrated with observational results and therefore they are more likely to reproduce the kinematic features observed in our universe.

We studied stellar particles inside a FoV of 20x20 kpc and divided the projected images into 40 bins of length 1kpc. We set the minimum number of stars to 25 and the target S/N to 10.

5.2. Kinematic measurement method selection

EKA provides V and σ values from the LOSVD and from the mean value and standard deviation of velocities from all the particles. The former provides higher values of V and σ closer to observations and thus we will use LOSVD results in the rest of the results shown in this section.

We have found that LOSVD present important differences whether they are mass or luminosity weighted. In Figure 2 we show the mass and luminosity weighted LOSVDs where these differences are clearly seen.

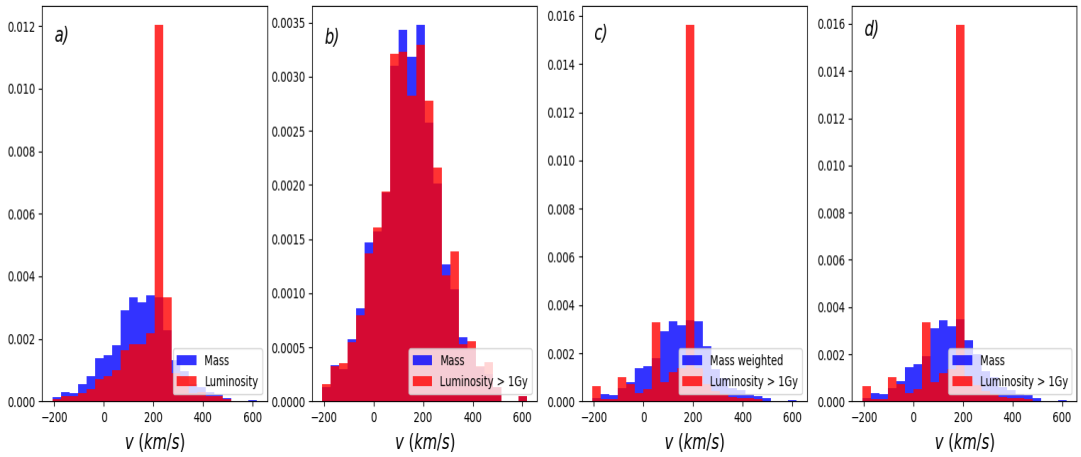

Figure 2. Mass (blue) and luminosity (red) weighted LOSVDs. The mass weighted LOSVDs are the same in the four subplots. Luminosity LOSVD: a) calculated from stellar population synthesis models including all the stars, b) calculated from stellar population synthesis models including stars older than 1Gy, c) calculated from g-band magnitudes in the database including all the stars, d) calculated from g-band magnitudes in the database including stars older than 1Gy.

These high values in the luminosity weighted LOSVD mean that there are stars with high mass to light ratios since this behaviour is not observed in the mass weighted LOSVD. First, we thought that these differences were produced by errors in the interpolation routine, but we checked that these discrepancies remain when using g-filter luminosities from magnitudes in the *Stars* database table in subfigure (b). In subfigures (c) and (d) we show the same LOSVDs including stars older than 1Gyr. It is clear that our interpolation method presents a strong dependence with stellar populations while the database luminosity is not affected. We will use our method because it provides almost the same results than the database luminosities when all the stars are included and we leave the stellar population dependence analysis for future works.

5.3. Kinematic maps

5.3.1. Comparison with other works in the literature

There are few works in the literature that focus on kinematical properties of EAGLE galaxies. In fact, there is only one work (Lagos et al 2018) that computes the kinematic maps and the $\lambda_R - \epsilon$ diagrams as far as we know. In the latter work the projected images are binned in pixels of 1.5 pkpc and V and σ are calculated by fitting a Gaussian to a r-band luminosity weighted LOSVD for each one of them.

In Figure 3 we visually compare the luminosity, velocity and velocity dispersions maps of two galaxies shown in Lagos et al. (2018) with our results. Our maps are not exactly equal but we are able to reproduce Lago's results to a great extent. Differences are caused by different image resolution and by different LOSVD fitting functions. Gaussian function only has the velocity dispersion to account of LOSVD asymmetries and it provides higher σ values than Gaus-Hermite function with LOSVD like in Figure 2.

5.3.2. RefL0100N1504 maps

We computed kinematical maps of all galaxies with stellar mass greater than $10^{10} M_{\odot}$ from the RefL0100N1504, and we found that most of the galaxies present regular rotation with aligned luminosity and kinematic axes. We have also found that EAGLE is able to reproduce more complex kinematic features like those found in observations. In Figure 4 we visually compare velocity and velocity dispersion maps obtained using *EKA* with maps from SAURON (Emsellem et al. 2004) and CALIFA (Tsatsi et al. 2007). EAGLE galaxies are identified by their *GalaxyID* and we observe four well differentiated kinematic features:

i) 9578504 and NGC 4486 are slow rotators. They present small velocity values with no distinct kinematic axis and high velocity dispersion values at the centre.

ii) 14151096 and NGC3377 are fast rotators. They show high velocity values and small velocity dispersion along the photometric major axis.

iii) 14916079 and NGC5831 are galaxies with corotation kinematic decoupled cores with high velocity values in the inner regions and almost no rotation outside; well visible in the velocity map.

iv) 15909288 and NGC6173 are long axis rotators. Their rotation axis is aligned with the photometric major axis.

Even when *EKA* and SAURON maps look very similar there are two aspects in which they differ. EAGLE galaxies with high central dispersion velocities show values around 200 km/s in edge on view and do not reach the 300 km/s and 400 km/s like NGC4374 and NGC4486 even in face on view. h_3 and h_4 maps range from -0.25 to 0.25 , which are the boundary conditions of the fit, and many pixels take these limit values suggesting their optimal values are even greater. On

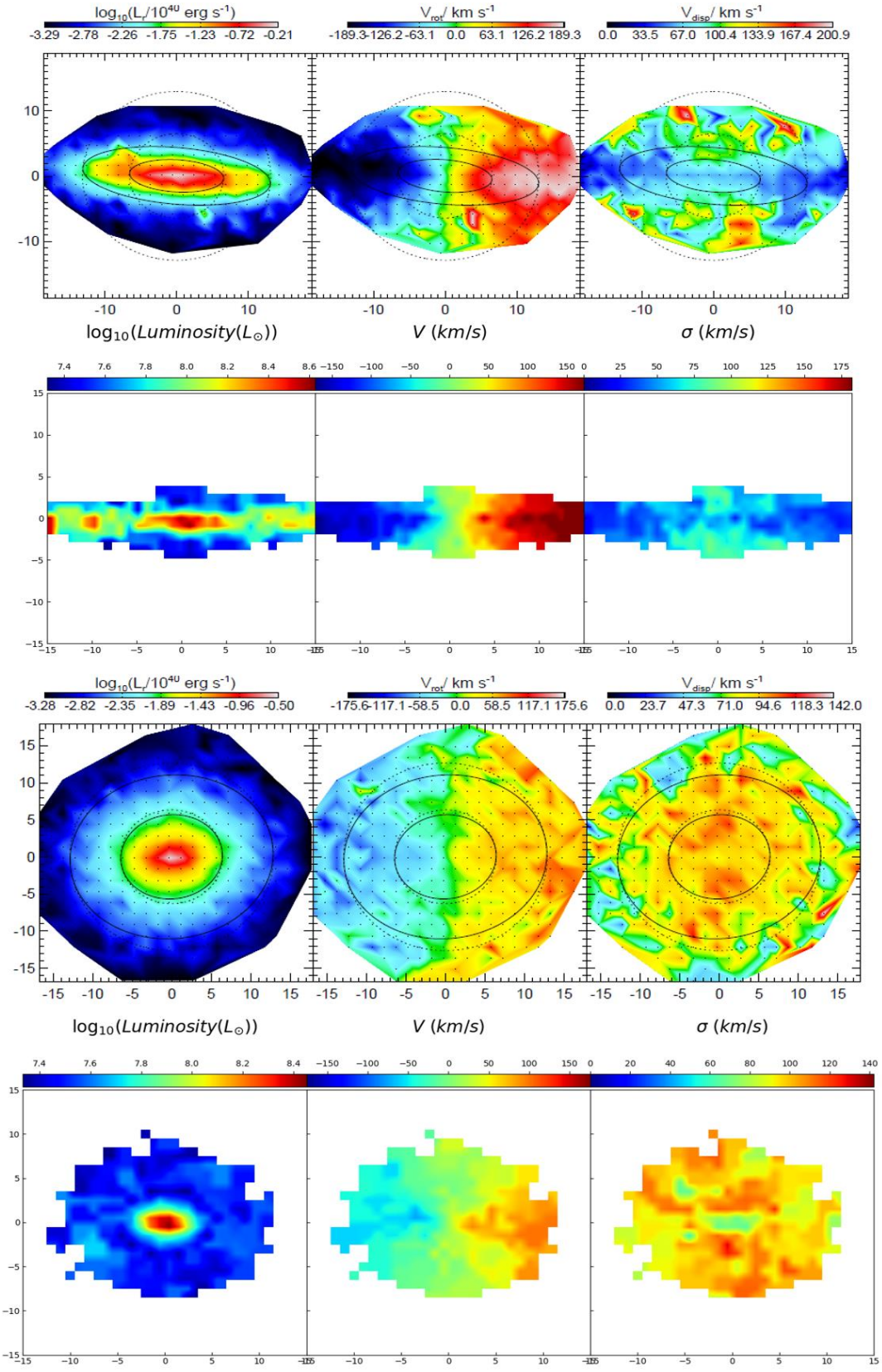

Figure 3. Comparison of edge on view luminosity (left), velocity (middle) and velocity dispersion (right) of two galaxies shown in Lagos et al. (2018), (first and third panels) and obtained using EKA scripts (second and fourth panels).

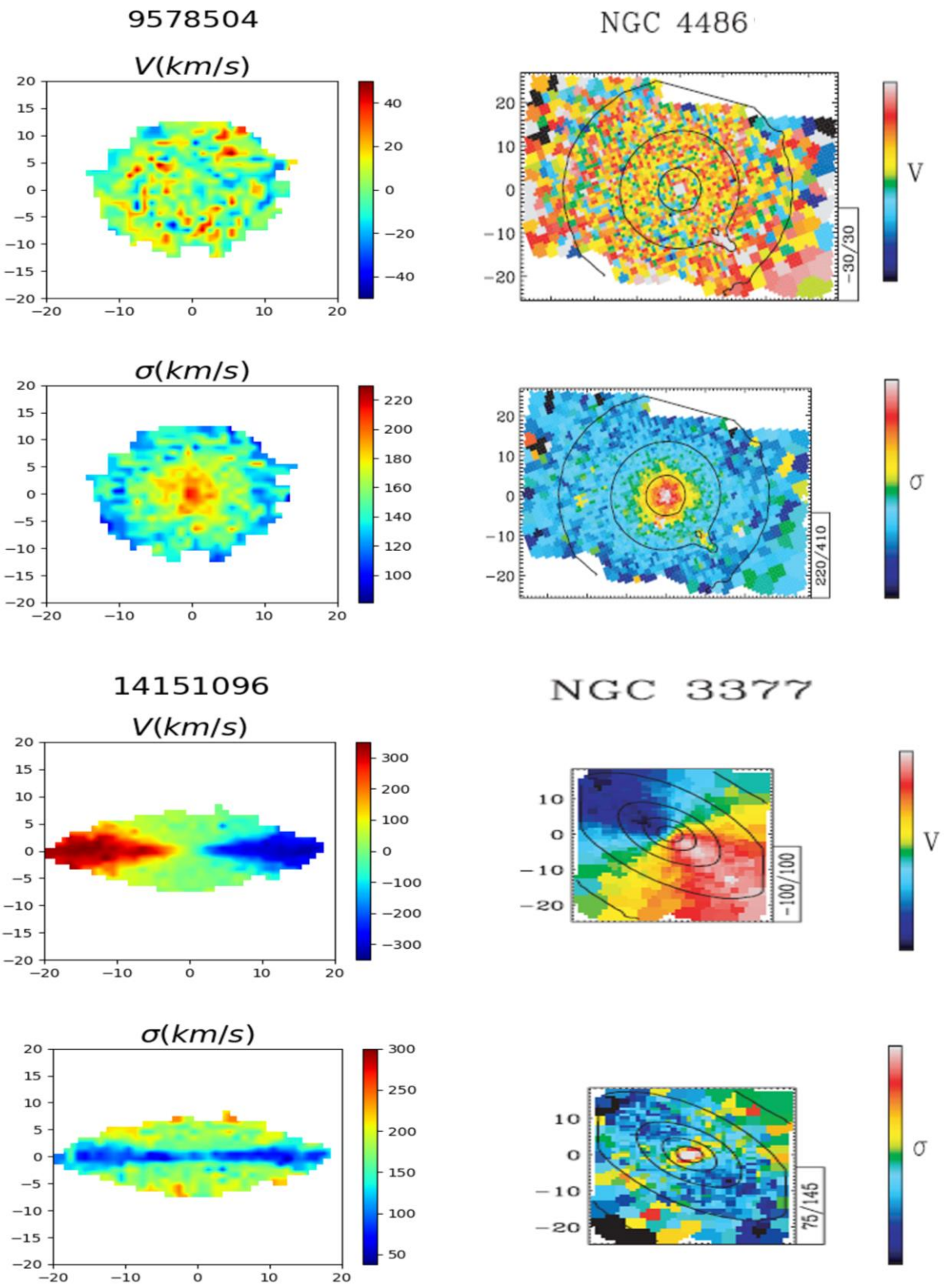

Figure 4, V and σ maps obtained using *EKA* and from SAURON survey Emsellem et al. (2004) and Tsatsi et al. (2007). The FoV units are kpc for EKA maps and arcsec for the observational results

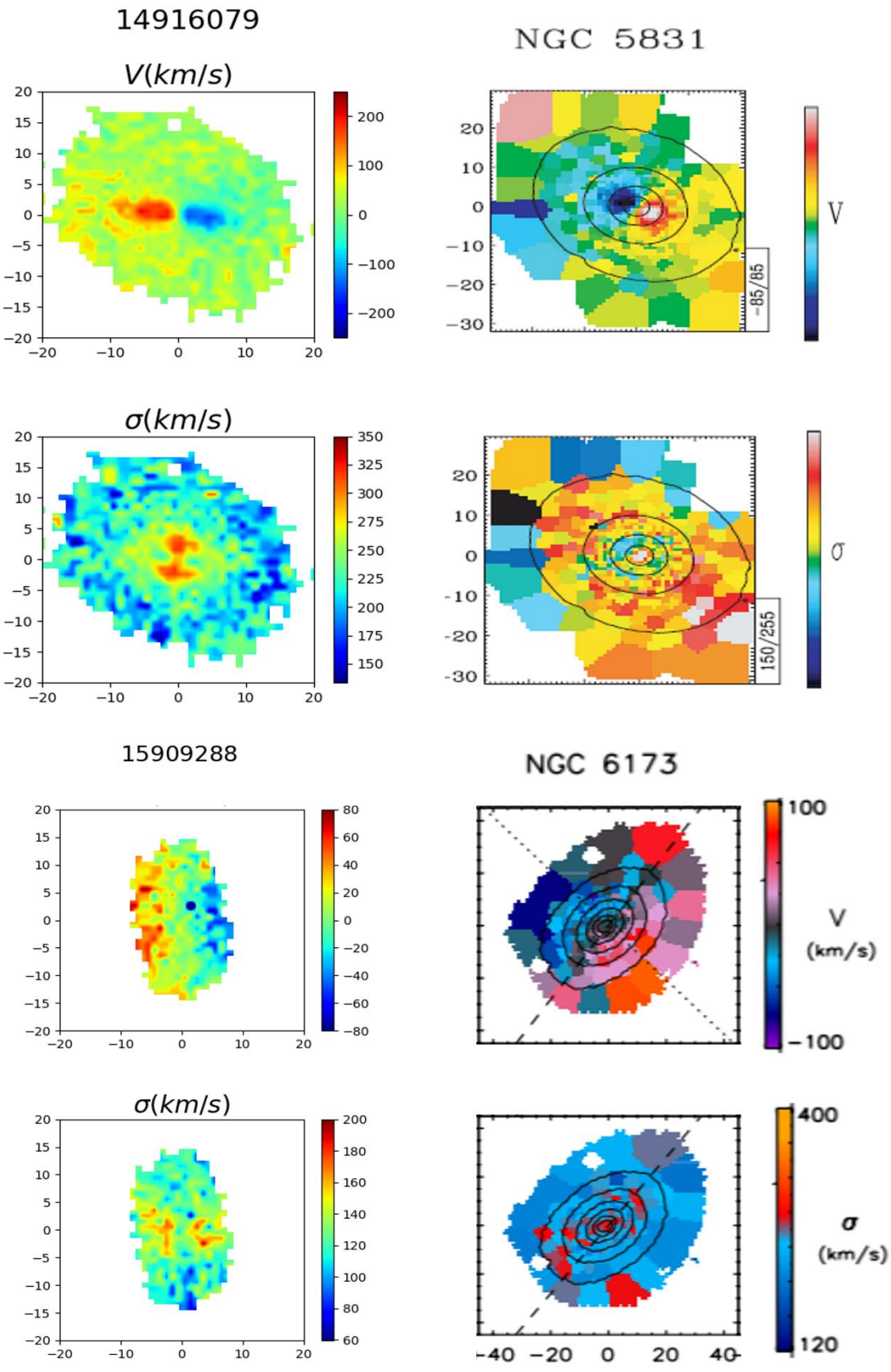

Figure 4. continued

the other hand, SAURON values range from -0.15 to 0.15 and the limit values are rarely reached. The origin of these differences comes from the kinematic extraction process. In SAURON they use deconvolution techniques (pPXF) to obtain the LOSVD from observed spectra and few high luminosity particles may not have great influence in the spectra. Therefore, the inferred LOSVD would not present sharp effects as ours. Additionally, observational results are limited by factors such as the quality of the signal, seeing and the resolution of the instrument that may limit h_3 and h_4 to smaller values. On the other hand, our results depend on the validity of luminosities to obtain the weighted LOSVD. We have already seen in Figure 3 that different methods do not provide exactly the same results and that further investigation to understand the influence of high luminosity particles is required.

5.4. Apparent angular momentum

To classify galaxies into fast and slow rotators observational surveys usually compare these magnitudes within apertures of radius R_{50}. The classification onto each group is performed based on the apparent angular momentum, λ_R, and ellipticity, ϵ. Following Emsellem et al. (2011) slow and fast rotators have λ_R lower and larger than $k_{FS} \times \sqrt{\epsilon}$, respectively, where $k_{FS} = 0.31$ for measurements within R_{50}. As we have mentioned in previous sections of this work, we calculate ϵ inside an annular mask of few kpc around R_{90} and λ_R elliptical apertures of major axis equal for both R_{50} and R_{90}. Figure 5 shows the $\lambda_R - \epsilon$ diagrams using $\lambda_{R_{50}}$ and $\lambda_{R_{90}}$ of galaxies from RefL100N1504 simulation in random view.

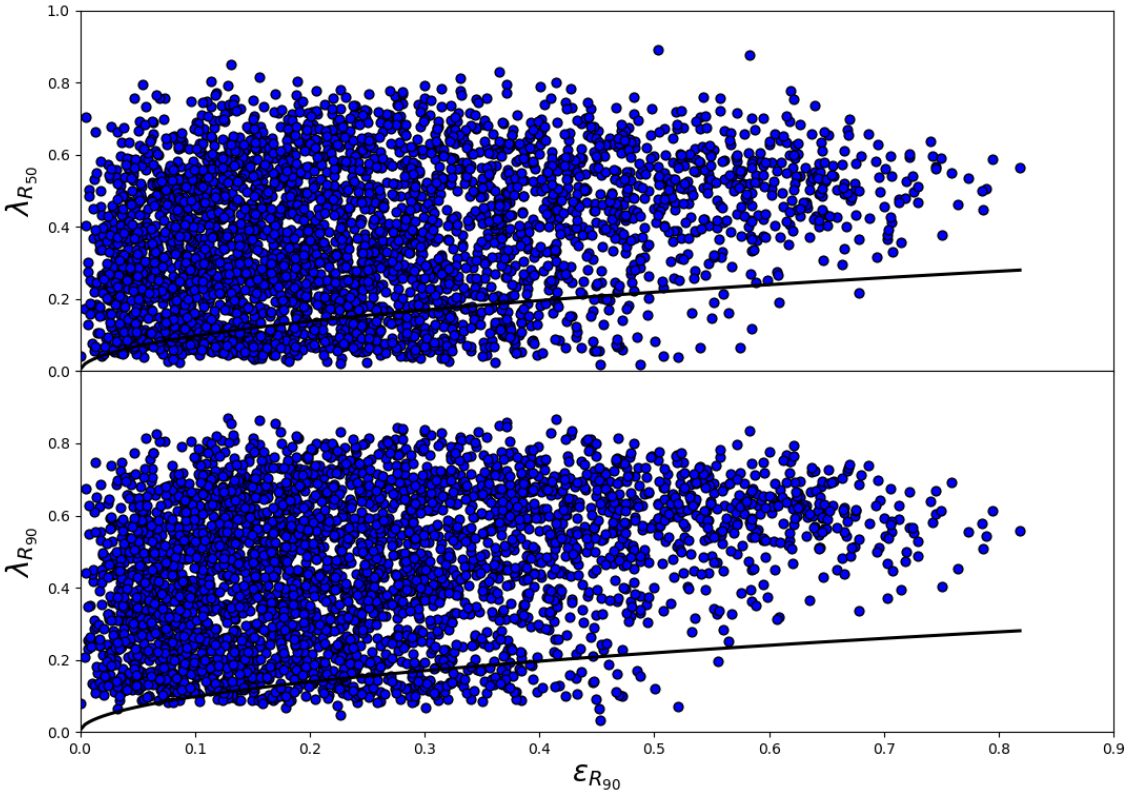

Figure 5: $\lambda_{R_{90}}$(top) and $\lambda_{R_{50}}$(bottom) as function of $\epsilon_{R_{90}}$ for galaxies in the simulation RefL0100N1504. the solid line shows the classification of slow and fast rotators from Emsellem et al. (2011).

We observe that both diagrams present almost the same structure and that extending the measuring area to R_{90} distributes the galaxies into a wider range of λ_R. We can appreciate that the region of λ_R from 0.6 to 0.8 is more populated in the second diagram, in particular for galaxies

with small $\epsilon_{R_{90}}$ showing that R_{50} is not enough to describe the kinematic properties of these galaxies. Additionally, there is a global displacement of minimum λ_R values from 0.04 to 0.08. In Figure 6, we observe that there is a linear positive correlation between $\lambda_{R_{90}}$and $\lambda_{R_{50}}$. There are some galaxies that do not follow this trend and present high $\lambda_{R_{90}}$ values for small $\lambda_{R_{50}}$ and would then become fast rotators using this analysis. These galaxies are very small and present small velocity dispersion region along the photometric major axis. On the other hand there are some galaxies with small velocity dispersion values at the centre regions and high values in the outer parts that present lambda $\lambda_{R_{90}}$ smaller than $\lambda_{R_{50}}$.

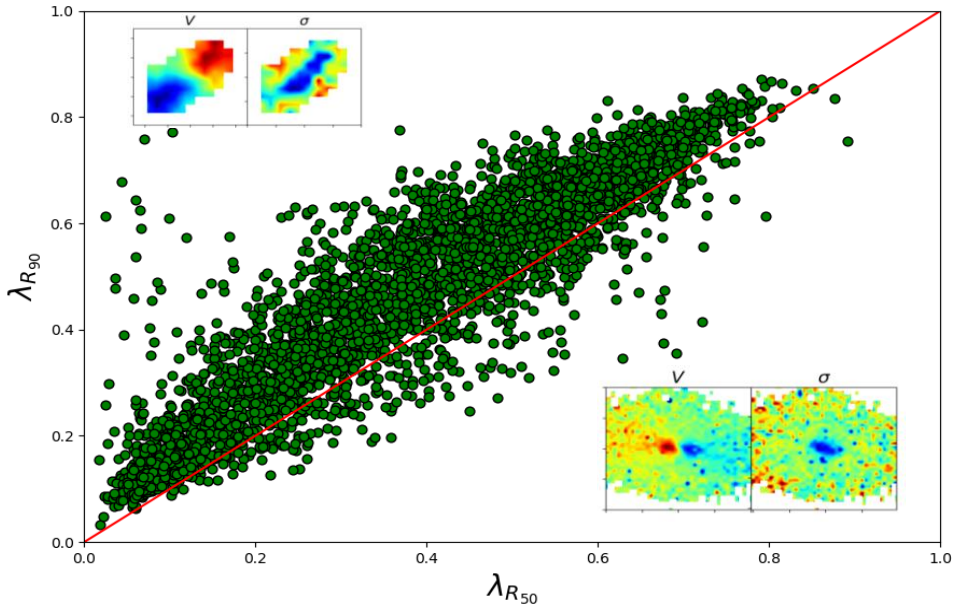

Figure 6. $\lambda_{R_{90}}$ as function of $\lambda_{R_{50}}$ for galaxies in the simulation RefL0100N1504. Red line represents the one-to-relation. Inset figures show the velocity and velocity dispersion maps of galaxies with small $\lambda_{R_{50}}$ and high $\lambda_{R_{90}}$ (top left) and high $\lambda_{R_{50}}$ and small $\lambda_{R_{90}}$ (bottom right)

In Figure 7 we compare the position of galaxies in the $\lambda_R - \epsilon$ diagrams from RefL0100N1504 using *EKA* results, with those calculated by Lagos et al. (2018) and from observational surveys ATLAS^{3D} (Emsellem et al. 2011), and CALIFA (Falcón-Barroso et al. 2014). We show λ_R and ϵ values measured within an elliptical mask of semimajor axis equal to R_{50} and inside an annular mask of few kpc around R_{90}, respectively. Both Lagos et al. (2018) and ATLAS^{3D} results calculate the λ_R and ϵ within elliptical an circular masks of semimajor axis and radius equal to R_{50}. In CALIFA, λ_R is measured within R_{50} but ϵ is measured similar to us in the outer regions of the galaxies. CALIFA diagram also show more galaxies with small λ_R and large ϵ values because they analyse galaxies across all the Hubble sequence while ATLAS^{3D} only analyse early type galaxies. Our $\lambda_R - \epsilon$ diagram is similar to the one shown in the bottom right panel of Figure 7, but present differences in both λ_R and ϵ caused by different spatial resolution, LOSVD fitting functions and size of the apertures in the ϵ calculation. Galaxies with ϵ values in the 0.6-0.8 range present smaller λ_R values in our diagram. We also observe that our analysis provides more galaxies with high λ_R and small ϵ. This feature is a direct consequence of the aperture size as we already showed in Figure 6. Both analysis lack the very high ellipticity galaxies with ellipticity values greater than 0.75 as can be observed in CALIFA and ATLAS^{3D} surveys. This may be due to the subgrid interstellar medium physics included in the simulations, which set a minimum disk height $\leq$ 1kpc (Lagos et al. 2018), larger than the Milky-Way or other spiral galaxies, which exhibit scale heights typically of $\approx$ 0.4 kpc (Kregel et al. 2002).

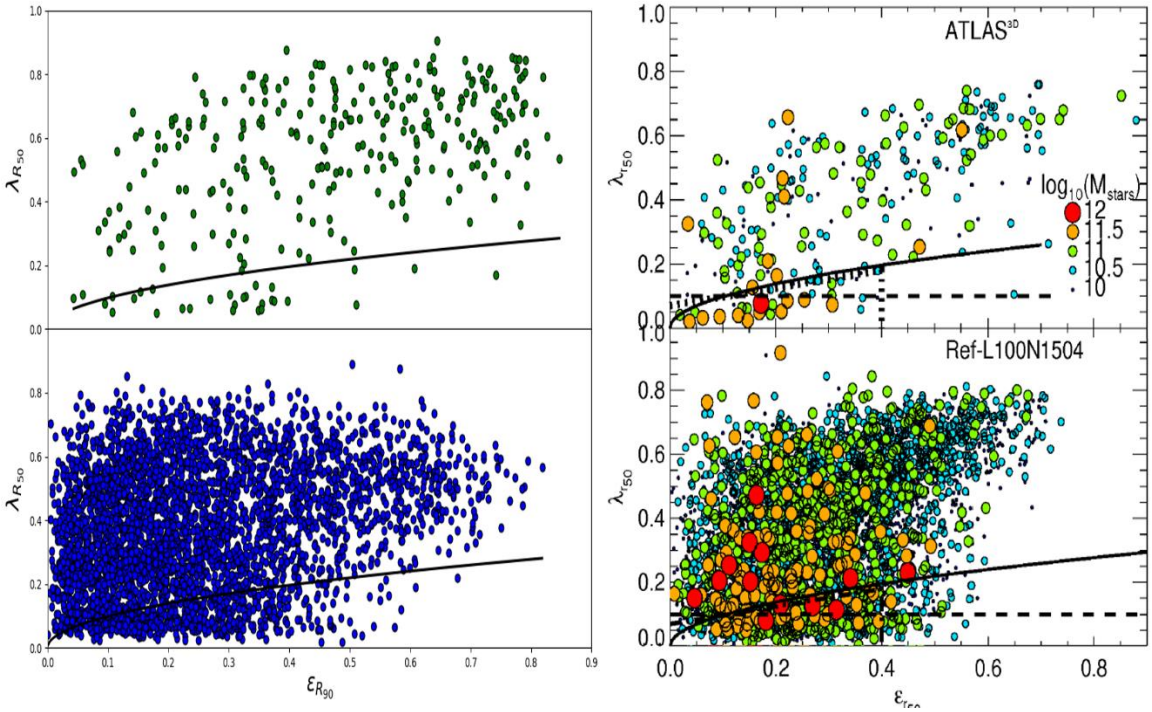

Figure 7. $\lambda_R - \epsilon$ diagrams in the CALIFA (Falcón-Barroso et al. 2014.;top left panel) and ATLAS^{3D} (Emsellem et al. 2011; top right panel) surveys and for the RefL0100N1504 simulation at redshift cero using *EKA* (bottom left panel) and from Lagos et al. (2018) (bottom right panel). Galaxies from RefL0100N1504 are random oriented in both analysis. In the four panels the solid line shows the classification of slow and fast rotators from Emsellem et al. (2011). ATLAS^{3D} and Lagos et al. (2018) diagrams also show another two classifications into fast and slow rotators from Emsellem et al. (2007) and Cappellari et al. (2016) as dashed and dotted lines, respectively.

We have classified the galaxies into bulge or disk dominated according to the fraction of kinetic energy invested in ordered rotation, κ_{corot}, as in Correa et al. (2017). We have found that using their criteria the upper regions of the $\lambda_R - \epsilon$ diagram is populated by disk galaxies while the lower one is occupied by bulge galaxies, as expected. However, the intermediate region of the diagram is populated by both types with no meaningful differences between them and no further information can be obtain from this approach.

We have also explored if the angular momentum is correlated with other parameters such as mean age, metallicity or [Mg/Fe]. The results were quite scattered and it was not possible to obtain a direct relation even when a faint general trend was appreciated. This result do not imply that these quantities are totally uncorrelated, but that a classification of galaxies into different groups and a more careful analysis is required. This analysis exceeds the aims of this work and is left for future studies.

5.5. λ_R evolution

We have studied galaxies with stellar mass larger than $10^{10}\,M_{\odot}$ in random view from snapshots 23 (z=0.5) and 19 (z=1) of RefL0100N1504 to analyse the evolution of kinematic properties through time.

In Figure 8 we show $\lambda_R - \epsilon$ diagrams for z=0, 0.5 and 1. We also plot the density maps of these diagrams to facilitate the analysis since the large number of galaxies studied in each snapshot makes it difficult to appreciate the differences between them.

We observe how the most densely populated regions of the diagram evolve through time. At z=1 there are more galaxies in the range of λ_R from 0.5 to 0.8 and ϵ between 0.1 and 0.7 while at z=0 the density map has substantially changed and there are more galaxies with lower λ_R and ϵ values. We also observe both in the $\lambda_R - \epsilon$ diagrams and in the density maps that at higher redshifts there are more galaxies with large ϵ and small λ_R.These changes are caused by galaxies mergers. The resulting angular momentum and morphology after merger interaction depend on several parameters such as stellar mass, inclination and angular momentum of the galaxies before collision, but on average this process tends to decrease the angular momentum and reduce the ellipticity of galaxies. This result show that most of slow rotators were originally fast rotators that have undergo merger processes. Additionally, we observe that density map changes more between z=0 to z=1 showing that these processes take place in the latter epochs of the universe.

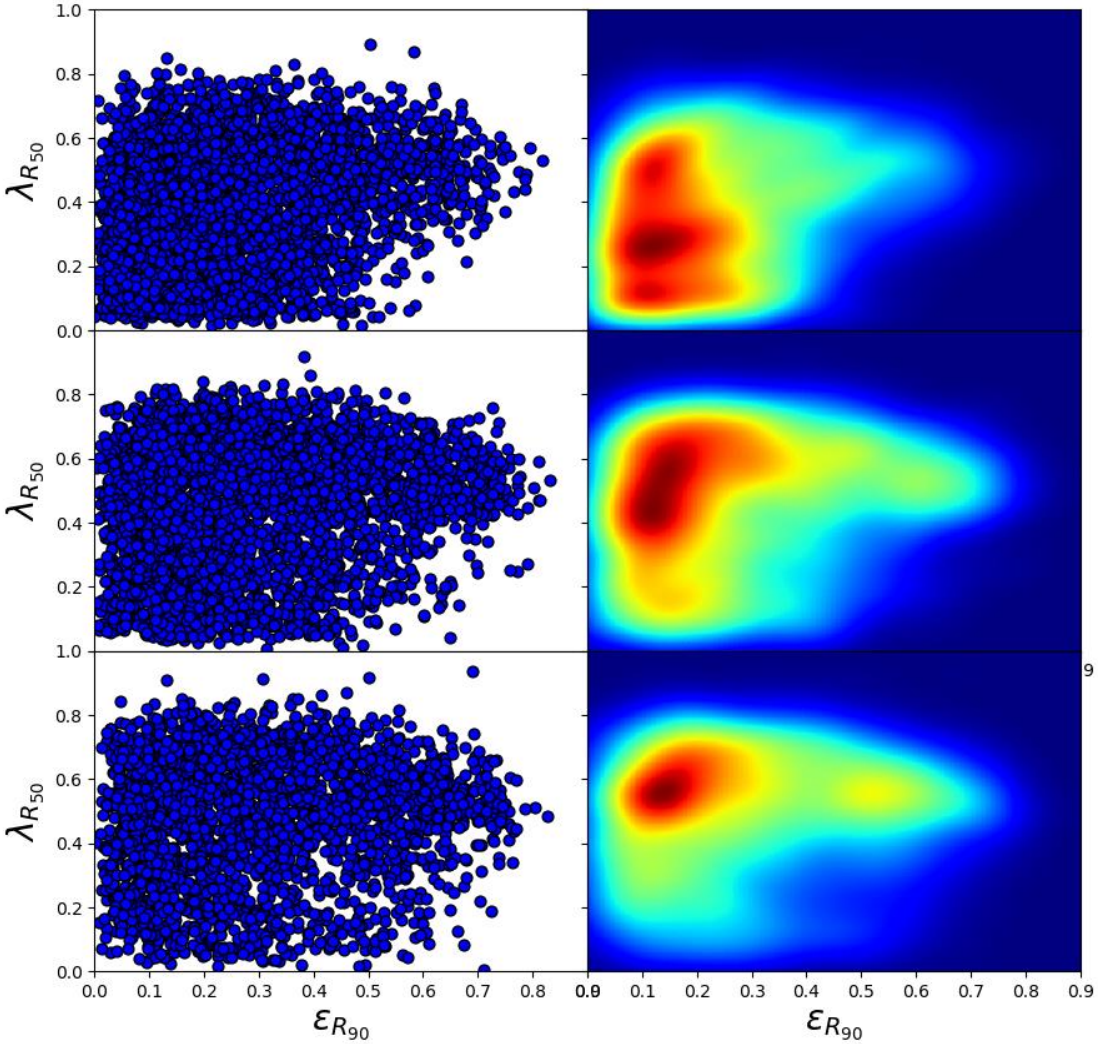

Figure 8. $\lambda_R - \epsilon$ diagrams and density maps of galaxies from RefL0100N1504 with stellar mass larger than $10^{10}\ M_{\odot}$ at different redshifts. From top to bottom: z=0, 0.5 and 1.

It is expected that the number of counter rotating stars in a galaxy increases through time as a consequence of mergers. In Figure 9 we show the distribution of the fraction of counter rotating trajectories, $N_{counter}$, and the fraction of kinetic energy invested in counter rotation, $\kappa_{counter}$.

These quantities have been calculated from stars inside a spherical aperture centred at centre of potential of radius 15 pkpc. We observe in both distributions that at z=0 there are more galaxies with higher values of $N_{counter}$ and $\kappa_{counter}$ than at higher redshift. We also see that the increase is similar in both distributions, showing that these quantities are directly correlated. We additionally plot $\kappa_{counter}$ as a function of $N_{counter}$ in the right panel of Figure 9 and observe that they are positive correlated. In fact, this correlation is almost the same at different redshifts. Most of the galaxy have $N_{counter}$ values between 0 and 0.5 and only few galaxies show that more than 50% of their trajectories are counter rotating.

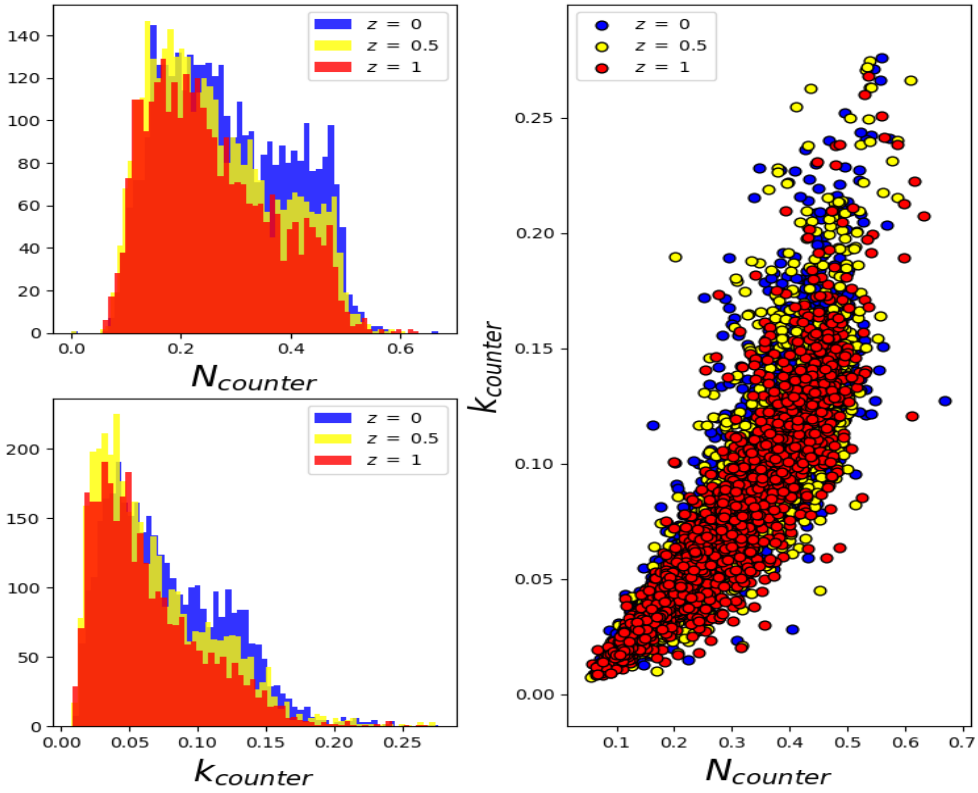

Figure 9. Distribution of $N_{counter}$ (top left panel) and $\kappa_{counter}$ (bottom left panel) for galaxies in random view from RefL0100N1504 simulation at different redshifts. $\kappa_{counter}$ as a function of $N_{counter}$ for different redshifts (right panel).

6. Conclusions

In this project we have developed EKA, a series of scripts that enables to analyse the kinematic properties of galaxies from EAGLE simulation in a simple way. We have used this new tool to analyse the galaxies in the RefL0100N1504 simulation at different redshifts. Most of the galaxies present regular rotation where the kinematic axis is aligned with the photometric axis. We have found that EAGLE is able to reproduce complex kinematic features such as long axis rotation or corotating kinematic decoupled cores. We have measured the apparent angular momentum, λ_R, and ellipticity, ϵ, and constructed the $\lambda_R - \epsilon$ diagram to analyse the distribution of slow and fast rotators. We have found that our results match those from other works in the literature that have studied the kinematic properties of EAGLE and that we are able to reproduce observational results from IFS surveys like ATLAS^{3D} and CALIFA. We have confirmed that on average galaxies become rounder, tend to loose angular momentum and increase the kinematic energy invested in counter rotation trough time due to galaxy mergers.

We have found some aspects of EAGLE particle data never seen before in the literature. First, we observed that the luminosity-weighted LOSVD present sharp effects irrespective of the method used to obtain the luminosities, but that some of them are more sensitive to stellar populations. Second, there are some stellar particles that present very large [Mg/Fe] for which we have not found a reasonable physical origin.

In conclusion, we have fully achieved the objectives of this project and we have discovered new features of EAGLE simulations to investigate in future works.

7. References

BOIS, Maxime, et al. The ATLAS3D project–VI. Simulations of binary galaxy mergers and the link with fast rotators, slow rotators and kinematically distinct cores. *Monthly Notices of the Royal Astronomical Society*, 2011, vol. 416, no 3, p. 1654-1679.

BRYANT, J. J., et al. The SAMI Galaxy Survey: instrument specification and target selection. *Monthly Notices of the Royal Astronomical Society*, 2015, vol. 447, no 3, p. 2857-2879.

CAPPELLARI, Michele; COPIN, Yannick. Adaptive spatial binning of integral-field spectroscopic data using Voronoi tessellations. *Monthly Notices of the Royal Astronomical Society*, 2003, vol. 342, no 2, p. 345-354.

CAPPELLARI, Michele; EMSELLEM, Eric. Parametric recovery of line-of-sight velocity distributions from absorption-line spectra of galaxies via penalized likelihood. *Publications of the Astronomical Society of the Pacific*, 2004, vol. 116, no 816, p. 138.

CAPPELLARI, Michele. Structure and kinematics of early-type galaxies from integral field spectroscopy. *Annual Review of Astronomy and Astrophysics*, 2016, vol. 54, p. 597-665.

CORREA, Camila A., et al. The relation between galaxy morphology and colour in the EAGLE simulation. *Monthly Notices of the Royal Astronomical Society: Letters*, 2017, vol. 472, no 1, p. L45-L49.

CROOM, Scott M., et al. The Sydney-AAO multi-object integral field spectrograph. *Monthly Notices of the Royal Astronomical Society*, 2012, vol. 421, no 1, p. 872-893.

DALLA VECCHIA, Claudio; SCHAYE, Joop. Simulating galactic outflows with kinetic supernova feedback. *Monthly Notices of the Royal Astronomical Society*, 2008, vol. 387, no 4, p. 1431-1444.

DUBOIS, Yohan, et al. The HORIZON-AGN simulation: morphological diversity of galaxies promoted by AGN feedback. *Monthly Notices of the Royal Astronomical Society*, 2016, vol. 463, no 4, p. 3948-3964.

DUBOIS, Yohan, et al. Dancing in the dark: galactic properties trace spin swings along the cosmic web. *Monthly Notices of the Royal Astronomical Society*, 2014, vol. 444, no 2, p. 1453-1468.

EAGLE team (2017) arXiv:1706.09899v1

EMSELLEM, Eric, et al. The SAURON project–III. Integral-field absorption-line kinematics of 48 elliptical and lenticular galaxies. *Monthly Notices of the Royal Astronomical Society*, 2004, vol. 352, no 3, p. 721-743

EMSELLEM, Eric, et al. The SAURON project–IX. A kinematic classification for early-type galaxies. *Monthly Notices of the Royal Astronomical Society*, 2007, vol. 379, no 2, p. 401-417.

EMSELLEM, Eric, et al. The ATLAS3D project–III. A census of the stellar angular momentum within the effective radius of early-type galaxies: Unveiling the distribution of Fast and Slow Rotators. *Monthly Notices of the Royal Astronomical Society*, 2011, vol. 414, no 2, p. 888-912.

FALCÓN-BARROSO, Jesús, et al. Angular Momentum across the Hubble sequence from the CALIFA survey. *Proceedings of the International Astronomical Union*, 2014, vol. 10, no S311, p. 78-81.

FURLONG, M., et al. Size evolution of normal and compact galaxies in the EAGLE simulation. *Monthly Notices of the Royal Astronomical Society*, 2016, p. stw2740.

FURLONG, M., et al. Evolution of galaxy stellar masses and star formation rates in the EAGLE simulations. *Monthly Notices of the Royal Astronomical Society*, 2015, vol. 450, no 4, p. 4486-4504.SCHREIBER, NM Förster, et al. The SINS survey: SINFONI integral field spectroscopy of z∼ 2 star-forming galaxies. *The Astrophysical Journal*, 2009, vol. 706, no 2, p. 1364.

GENEL, Shy, et al. Introducing the Illustris project: the evolution of galaxy populations across cosmic time. *Monthly Notices of the Royal Astronomical Society*, 2014, vol. 445, no 1, p. 175-200.

KREGEL, Michiel; VAN DER KRUIT, Pieter C.; DE GRIJS, Richard. Flattening and truncation of stellar discs in edge-on spiral galaxies. *Monthly Notices of the Royal Astronomical Society*, 2002, vol. 334, no 3, p. 646-668.

KATSIANIS, A., et al. The evolution of the star formation rate function in the EAGLE simulations: a comparison with UV, IR and Hα observations from∼ to∼. *Monthly Notices of the Royal Astronomical Society*, 2017, vol. 472, no 1, p. 919-939.

JESSEIT, Roland, et al. Specific angular momentum of disc merger remnants and the λR-parameter. *Monthly Notices of the Royal Astronomical Society*, 2009, vol. 397, no 3, p. 1202-1214.

DOLAG, K., et al. Substructures in hydrodynamical cluster simulations. *Monthly Notices of the Royal Astronomical Society*, 2009, vol. 399, no 2, p. 497-514.

LAGOS, Claudia del P., et al. Quantifying the impact of mergers on the angular momentum of simulated galaxies. *Monthly Notices of the Royal Astronomical Society*, 2017, vol. 473, no 4, p. 4956-4974.

LAGOS, Claudia del P., et al. The connection between mass, environment, and slow rotation in simulated galaxies. *Monthly Notices of the Royal Astronomical Society*, 2018, vol. 476, no 4, p. 4327-4345.

LINTOTT, Chris, et al. Galaxy Zoo 1: data release of morphological classifications for nearly 900 000 galaxies. *Monthly Notices of the Royal Astronomical Society*, 2010, vol. 410, no 1, p. 166-178.

MCALPINE, Stuart, et al. The EAGLE simulations of galaxy formation: public release of halo and galaxy catalogues. *Astronomy and Computing*, 2016, vol. 15, p. 72-89.

MO, H. J.; MAO, Shude; WHITE, Simon DM. The formation of galactic discs. *Monthly Notices of the Royal Astronomical Society*, 1998, vol. 295, no 2, p. 319-336.

NAAB, Thorsten, et al. The ATLAS3D project–XXV. Two-dimensional kinematic analysis of simulated galaxies and the cosmological origin of fast and slow rotators. *Monthly Notices of the Royal Astronomical Society*, 2014, vol. 444, no 4, p. 3357-3387.

Planck Collaboration. ADE, Peter AR, et al. Planck 2013 results. I. Overview of products and scientific results. *Astronomy & Astrophysics*, 2014, vol. 571, p. A1.

ROSAS-GUEVARA, Y. M., et al. The impact of angular momentum on black hole accretion rates in simulations of galaxy formation. *Monthly Notices of the Royal Astronomical Society*, 2015, vol. 454, no 1, p. 1038-1057.

PILLEPICH, Annalisa, et al. Simulating galaxy formation with the IllustrisTNG model. *Monthly Notices of the Royal Astronomical Society*, 2017, vol. 473, no 3, p. 4077-4106.SÁNCHEZ, Sebastián F., et al. CALIFA, the Calar Alto Legacy Integral Field Area survey-I. Survey presentation. *Astronomy & Astrophysics*, 2012, vol. 538, p. A8.

SCHAYE, Joop; DALLA VECCHIA, Claudio. On the relation between the Schmidt and Kennicutt–Schmidt star formation laws and its implications for numerical simulations. *Monthly Notices of the Royal Astronomical Society*, 2008, vol. 383, no 3, p. 1210-1222.

SCHAYE, Joop, et al. The EAGLE project: simulating the evolution and assembly of galaxies and their environments. *Monthly Notices of the Royal Astronomical Society*, 2014, vol. 446, no 1, p. 521-554.

SHARPLES, Ray, et al. Design of the KMOS multi-object integral-field spectrograph. En *Ground-based and Airborne Instrumentation for Astronomy*. International Society for Optics and Photonics, 2006. p. 62691C.

SHEN, Shiyin, et al. The size distribution of galaxies in the Sloan Digital Sky Survey. *Monthly Notices of the Royal Astronomical Society*, 2003, vol. 343, no 3, p. 978-994.

SNYDER, Gregory F., et al. Galaxy morphology and star formation in the Illustris Simulation at z= 0. *Monthly Notices of the Royal Astronomical Society*, 2015, vol. 454, no 2, p. 1886-1908.SWINBANK, A. M., et al. Angular momentum evolution of galaxies over the past 10 Gyr: a MUSE and KMOS dynamical survey of 400 star-forming galaxies from z= 0.3 to 1.7. *Monthly Notices of the Royal Astronomical Society*, 2017, vol. 467, no 3, p. 3140-3159.

TRAYFORD, James W., et al. Colours and luminosities of z= 0.1 galaxies in the EAGLE simulation. *Monthly Notices of the Royal Astronomical Society*, 2015, vol. 452, no 3, p. 2879-2896.

TSATSI, Athanasia, et al. CALIFA reveals prolate rotation in massive early-type galaxies: A polar galaxy merger origin?. *Astronomy & Astrophysics*, 2017, vol. 606, p. A62.

VAN DER MAREL, Roeland P., et al. A new method for the identification of non-Gaussian line profiles in elliptical galaxies. *Astrophysical Journal*, 1993, vol. 407, p. 525.

VAZDEKIS, A., et al. Evolutionary stellar population synthesis with MILES–I. The base models and a new line index system. *Monthly Notices of the Royal Astronomical Society*, 2010a, vol. 404, no 4, p. 1639-1671.

WIERSMA, Robert PC; SCHAYE, Joop; SMITH, Britton D. The effect of photoionization on the cooling rates of enriched, astrophysical plasmas. *Monthly Notices of the Royal Astronomical Society*, 2009, vol. 393, no 1, p. 99-107.

WIERSMA, Robert PC, et al. Chemical enrichment in cosmological, smoothed particle hydrodynamics simulations. *Monthly Notices of the Royal Astronomical Society*, 2009, vol. 399, no 2, p. 574-600.

8.0Appendix A

Parameter name	Description
C9050_Lum	Concentration parameter calculated from luminosity map
C9050_Mass	Concentration parameter calculated from luminosity map
DescendantID	*GalaxyID* of the unique descendat galaxy of a selected galaxy
GalaxyLuminosity	Total luminosity of the galaxy
GalaxyMass_BlackHoles	Total black hole mass
GalaxyMass_DarkMatter	Total dark matter mass
GalaxyMass_Gas	Total gas mass
GalaxyMass_Star	Total stellar mass
GalaxyMass_Total	Total mass of the galaxy
GroupNumber	FoF halo identifier number
K_corot	Fraction of kinetic energy invested in ordered rotation of particles that follow the direction of rotation
K_counterRot	Fraction of kinetic energy invested in ordered rotation of particles that rotate in the opposite direction of the direction of rotation
LastProgID	Maximum *GalaxyID* of all progenitors irrespective of their branch
MeanAge50_Lum	Luminosity weighted mean age inside elliptical apertures of major axis R50
MeanAge50_Mass	Mass weighted mean age inside elliptical apertures of major axis R50
MeanAge90_Lum	Luminosity weighted mean age inside elliptical apertures of major axis R90
MeanAge90_Mass	Mass weighted mean age inside elliptical apertures of major axis R90
MeanMgFe50_Lum	Luminosity weighted mean [Mg/Fe] inside elliptical apertures of major axis R50
MeanMgFe50_Mass	Mass weighted mean [Mg/Fe] inside elliptical apertures of major axis R50
MeanMgFe90_Lum	Luminosity weighted mean [Mg/Fe] inside elliptical apertures of major axis R90
MeanMgFe90_Mass	Mass weighted mean [Mg/Fe] inside elliptical apertures of major axis R90
MeanZ50_Lum	Luminosity weighted mean Z inside elliptical apertures of major axis R50

Table A1. List of parameters stored in the General_Output group of *EK*A's outputfile

Parameter name	Description
MeanZ50_Mass	Mass weighted mean Z inside elliptical apertures of major axis R50
MeanZ90_Lum	Luminosity weighted mean Z inside elliptical apertures of major axis R90
MeanZ90_Mass	Mass weighted mean Z inside elliptical apertures of major axis R90
R50_Lum	Projected half luminosity radius of stellar component
R50_Mass	Projected half mass radius of stellar component
R90_Lum	Projected 90% luminosity radius of stellar component
R90_Mass	Projected 90% mass radius of stellar component
StelarFormationRate	Total star formation rate
SubGroupNumber	Identifier number of a self-bound structure in a FoF halo
TopLeafID	*GalaxyID* of the highest-redshift main branch progenitor
Ellipticity50_Lum	Apparent ellipticity measured within R_{50} in the luminosity map
Ellipticity50_Mass	Apparent ellipticity measured within R_{50} in the mass map
Ellipticity90_Lum	Apparent ellipticity measured within R_{90} in the luminosity map
Ellipticity90_Mass	Apparent ellipticity measured within R_{90} in the mass map
GalaxyID	Unique identifier of a galaxy
LambdaR50_Lum	Apparent ellipticity measured within R_{50} in the luminosity map and kinematic parameters from LOSVD
LambdaR50_Mass	Apparent ellipticity measured within R_{50} in the mass map and kinematic parameters from LOSVD
LambdaR50_Numeric_ Lum	Apparent ellipticity measured within R_{50} in the luminosity map and kinematic parameters from averaged values
LambdaR50_Numeric_ Mass	Apparent ellipticity measured within R_{50} in the mass map and kinematic parameters from averaged values
LambdaR90_Lum	Apparent ellipticity measured within R_{90} in the luminosity map and kinematic parameters from LOSVD
LambdaR90_Mass	Apparent ellipticity measured within R_{90} in the mass map and kinematic parameters from LOSVD
LambdaR90_Numeric_ Lum	Apparent ellipticity measured within R_{90} in the luminosity map and kinematic parameters from averaged values

Table A1. Continued

Parameter name	**Description**
LambdaR90_Numeric_ Mass	Apparent ellipticity measured within R_{90} in the mass map and kinematic parameters from averaged values
Theta50_Lum	Position angle of the major semiaxis of ellipses in the luminosity map at R_{50}
Theta50_Mass	Position angle of the major semiaxis of ellipses in the mass map at R_{50}
Theta90_Lum	Position angle of the major semiaxis of ellipses in the luminosity map at R_{90}
Theta90_Mass	Position angle of the major semiaxis of ellipses in the mass map at R_{90}

Table A1. Continued

Map name	Description
h3_Lum	h3 obtained from luminosity weighted LOSVD
h3_Mass	h3 obtained from mass weighted LOSVD
h4_Lum	h4 obtained from luminosity weighted LOSVD
h4_Mass	h4 obtained from mass weighted LOSVD
Lum	Luminosity
Mass	Mass
MeanAge_Lum	Luminosity-weighted mean stellar age
MeanAge_Mass	Mass-weighted mean stellar age
MeanZ_Lum	Luminosity-weighted mean metallicity
MeanZ_Mass	Mass-weighted mean metallicity
MeanMgFe_Lum	Luminosity-weighted mean magnesium over iron
MeanMgFe_Mas	Mass-weighted mean magnesium over iron
Nstars	Number of stars
Sigma _Lum	Velocity-dispersion obtained from luminosity-weighted LOSVD
Sigma _Mass	Velocity dispersion obtained from mass-weighted LOSVD
Sigma _Numeric_Lum	Velocity dispersion obtained from luminosity-weighted standard deviation
Sigma_Numeric_Mass	Velocity dispersion obtained from mas-weighted standard deviation
Velocity_Lum	Velocity dispersion obtained from luminosity-weighted LOSVD
Velocity_Mass	Mean velocity dispersion obtained from mass-weighted LOSVD
Velocity_Numeric_Lum	Mean Velocity dispersion obtained from-luminosity weighted standard deviation
Velocity_Numeric_Mass	Velocity dispersion obtained from mass weighted-standard deviation
X	X coordinate of pixels in the projected maps
Y	Y coordinate of pixels in the projected maps

Table A2. List of maps stored for each galaxy in the *Maps* group of *EKA*'s ouput file.